Chapter 19
Recent Progress in Frequency Modulation Atomic Force Microscopy in Liquids

Kei Kobayashi and Hirofumi Yamada

Abstract Recent progress in frequency modulation atomic force microscopy (FM-AFM) working in liquids has allowed us to directly investigate a wide variety of physical, chemical and biological processes at molecular scale, including various "in vivo" biological interactions. In particular, two/three-dimensional (2D/3D) force mapping based on quantitative FM-AFM force measurements has been applied to various solid-liquid interface studies on a molecular scale. In this chapter, after a brief overview of FM-AFM working in liquids, crucial conditions required for quantitative force measurement are described. In addition we show the applications of 2D/3D force mapping to the visualization of molecular-scale hydration structures as well as that of local electric double layer forces. Finally high-resolution FM-AFM images of biological molecules such as double-helix structure of DNA and immunoglobulin G (IgG) antibody molecules obtained in quasi-physiological environments are presented.

19.1 Brief Overview

19.1.1 Introduction

Solid-liquid interfaces play a critical role in a large variety of physical, chemical and biological processes, such as crystal growth, catalytic reactions and various biochemical functions. Investigations of molecular-scale structures and interactions at solid-liquid interfaces are, therefore, essentially crucial for understanding theses microscopic processes. Recent, significant progress in frequency modulation atomic

H. Yamada (✉)
Department of Electronic Science and Engineering, Kyoto University,
Katsura, Nishikyo, Kyoto 615-8510, Japan
e-mail: h-yamada@kuee.kyoto-u.ac.jp

K. Kobayashi
The Hakubi Center for Advanced Research, Kyoto University,
Katsura, Nishikyo, Kyoto 615-8520, Japan
e-mail: keicoba@iic.kyoto-u.ac.jp

S. Morita et al. (eds.), *Noncontact Atomic Force Microscopy*,
NanoScience and Technology, DOI 10.1007/978-3-319-15588-3_19

force microscopy (FM-AFM) [1] working in liquids has allowed us to directly study such molecular-scale processes, including various "in vivo" biological interactions. In this article, after the characteristic features in solid-liquid interface measurements by FM-AFM are briefly mentioned, essential conditions required for quantitative force measurement in liquids are explained, which is essentially important for the interaction force analysis based on two/three-dimensional (2D/3D) force mapping [2–4]. In fact the method was successfully applied to the visualization of 2D/3D molecular-scale hydration structures at solid-liquid interfaces [2, 3] as well as those around biomolecules [4]. It was also applied to the visualization of local electric double layer (EDL) forces on molecular assemblies in electrolyte solution [5]. The quantitative force measurement allows us to obtain the molecular-scale surface charge density utilizing a modified DLVO (Derjaguin, Landau, Verwey and Overbeek) theory. Furthermore, some recent results on high-resolution FM-AFM imaging of biomolecules in quasi-physiological environments [5, 6] are also presented.

19.1.2 Characteristic Features in FM-AFM Solid-Liquid Interface Measurements

19.1.2.1 Viscous Damping of Cantilever in Fluid

In liquid environments the oscillation of the AFM cantilever is heavily damped by the fluid resistance so that the quality factor (Q-factor) of the cantilever is extremely reduced. This large reduction in Q-factor causes a large increase in frequency noise and hence deteriorates FM-AFM imaging. Sader and co-workers introduced dimensionless "hydrodynamic function" Γ [8, 9] having both real and imaginary parts ($\Gamma = \Gamma_r + i\Gamma_i$) for expressing the amplitude transfer function, $A(\omega)$, of the cantilever oscillation in liquids. When the cantilever has a rectangular shape with a width b, a thickness h and a density ρ, $A(\omega)$ is expressed by

$$A(\omega) = \frac{{\omega_{0(\mathrm{liq})}}^2}{-\omega^2 + {\omega_{0(\mathrm{liq})}}^2 + i\omega\omega_{0(\mathrm{liq})}/Q_{\mathrm{liq}}} A_{\mathrm{d}}, \tag{19.1}$$

where

$${\omega_{0(\mathrm{liq})}}^2 = \frac{1}{1 + \left(\pi\rho_{\mathrm{liq}} b/4\rho h\right)\Gamma_r}{\omega_0}^2 \text{ and } Q_{\mathrm{liq}} = \frac{\left(4\rho h/\pi\rho_{\mathrm{liq}} b\right) + \Gamma_r}{\Gamma_i}. \tag{19.2}$$

Here A_d and ρ_{liq} are the drive amplitude and the liquid density, respectively. These equations describe the reduction in Q-factor (Q_{liq}) caused by the viscous resistance as well as the decrease of the resonance frequency ($\omega_{0(\mathrm{liq})}$) due to the increase of the effective mass. Using the following modified Reynolds number Re,

$$\mathrm{Re} = \frac{\rho_{\mathrm{liq}}\omega b^2}{4\mu}, \tag{19.3}$$

where μ is the liquid viscosity, Γ can be approximated by using [8, 10]

$$\Gamma_r = a_1 + \frac{a_2}{\sqrt{2\,\mathrm{Re}}} \text{ and } \Gamma_i = \frac{b_1}{\sqrt{2\,\mathrm{Re}}} + \frac{b_2}{2\,\mathrm{Re}}, \tag{19.4}$$

where $a_1 = 1.0553$, $a_2 = 3.7997$, $b_1 = 3.8018$, $b_2 = 2.7364$. For a rectangular Si cantilever with $b = 35\,\mu\mathrm{m}$, $L = 125\,\mu\mathrm{m}$, and $h = 3.8\,\mu\mathrm{m}$ ($k = 42\,\mathrm{N/m}$, $f_0 = 335\,\mathrm{kHz}$), the approximation gives $Q_{\mathrm{liq}} = 10$ and $f_{0(\mathrm{liq})} = 155\,\mathrm{kHz}$. These numbers are close to the measured values, $Q_{\mathrm{liq}} = 7$–8, $f_{0(\mathrm{liq})} = 150\,\mathrm{kHz}$.

19.1.2.2 Frequency Noise in FM-AFM in Liquids

In FM-AFM the cantilever is vibrated at its resonance frequency f_0 with an oscillation amplitude A by the FM-AFM electronics. When the interaction forces act on the cantilever, the resonance frequency is shifted by a frequency shift Δf (frequency shift). In a high-Q environment such as in vacuum, the frequency noise density $n_{\delta f}^{(\text{high-}Q)}$ [Hz/$\sqrt{\text{Hz}}$] is expressed as

$$n_{\delta f}^{(\text{high-}Q)} = \frac{1}{A}\sqrt{\frac{f_0 k_\mathrm{B} T}{\pi k Q} + 2N_{\mathrm{ds}}^2 {f_\mathrm{m}}^2}, \tag{19.5}$$

where k, Q, k_B, and T are the spring constant, the Q-factor, the Boltzmann constant and the temperature, respectively [1]. f_m and N_{ds} denote the modulation frequency [Hz] and the displacement noise density of the deflection sensor [m/$\sqrt{\text{Hz}}$], respectively. The first term is the intrinsic frequency noise of the cantilever, which is caused by the thermal Brownian motion. The second term shows the well-known FM noise. In contrast, the frequency fluctuation of the oscillator has to be considered in a low-Q environment such as in water. In fact we recently found [11] that the frequency noise density in the low-Q environment $n_{\delta f}^{(\text{low-}Q)}$ is expressed as

$$n_{\delta f}^{(\text{low-}Q)} = \frac{1}{A}\sqrt{\frac{f_0 k_\mathrm{B} T}{\pi k Q} + \frac{f_0^2 N_{\mathrm{ds}}}{2Q^2}}. \tag{19.6}$$

Since f_0/Q is much larger than f_m in liquids, the magnitude of the second term of the above equation is much larger than that of (19.5). Thus, the reduction of the deflection sensor noise N_{ds} is essentially important. The noise was actually reduced by decreasing the coherence of the laser light used in the optical beam deflection sensor [12].

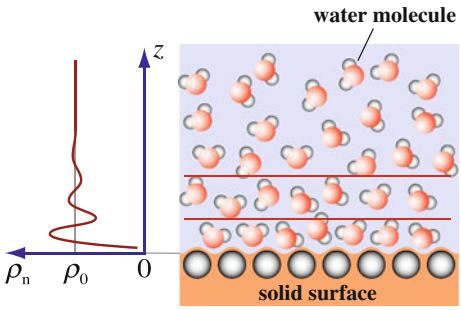

Fig. 19.1 Schematic of hydration structure formed on a flat solid surface. Molecule number density (ρ_n) plotted against z-distance (z) shows an oscillatory curve with an approximate period of the water molecule size (*left*)

19.1.2.3 Solvation (Hydration) Force

While liquid is treated as uniform continuum in fluid dynamics, the size effect of the liquid molecule has to be considered on a molecular scale. For instance, liquid density around an arbitrarily chosen single molecule cannot be uniform because of preferential coordination of neighboring molecules, which is described as density distribution function. This is also the case with the density distribution at a liquid-solid interface, which is known as solvation (hydration) structure (see Fig. 19.1). Typical molecule density distribution shows a diminishing oscillation structure with an approximate periodicity of the molecule size. Since force (frequency shift) versus distance curves were found to directly reflect the hydration structures formed at solid-liquid interfaces, 2D/3D force mapping has been applied to the study of molecular-scale hydration structures. When the tip is sufficiently sharp and hydrated, it can be treated as a water molecule tip, which makes the theoretical relationship between the measured force $F_{ts}(z)$ and the local molecule number density $\rho_n(z)$ extremely simple as follows [13],

$$F_{ts}(z) = k_B T \frac{d \log \rho_n(z)}{dz}. \tag{19.7}$$

However, the quantitative relationship between them is generally not straightforward because the interaction force acting on the tip caused by the hydration structure is strongly affected by the tip geometry and the hydration structure on the tip side, which requires careful theoretical calculation using molecular dynamics (MD) simulation or 3D reference interaction site model (RISM) theory [14].

19.1.2.4 Electric Double Layer Force

Sample surface is often charged in liquid due to the ionization of surface groups and/or ion absorption and the resultant local electrostatic force extremely complicates the interpretation. Surface charge is electrically balanced by the counter ions existing in the proximity of the surface so that an electric double layer is formed on the

surface (diffused double layer). An electric double layer also exists on the tip surface. When the tip is brought into close proximity of the sample surface, an interaction is caused between both electric double layers (electric double layer force). EDL force is the addition of Maxwell stress, electrostatic interaction, and osmotic pressure, statistical effect. Electrostatic potential in an electrolyte solution is $\phi(\mathbf{r})$ described by the following Poisson-Boltzmann equation,

$$\nabla^2\phi(\mathbf{r}) = \frac{Zen_0}{\varepsilon}\kappa^2 \sinh\left[Ze\phi(\mathbf{r})/k_\mathrm{B}T\right] \tag{19.8}$$

with

$$\kappa^{-1} = \sqrt{\frac{\varepsilon k_\mathrm{B}T}{2n_\mathrm{ion}\,(Ze)^2}}, \tag{19.9}$$

where n_ion, Z, e and ε are ion density, ion valence, elementary charge and dielectric constant of the solution, respectively. κ^{-1} is so called the Debye screening length corresponding to the thickness of the electric double layer in a simple system such as planar, parallel plates. When $e\phi \ll k_\mathrm{B}T$ and the system can be approximated as parallel plate, the equation can be solved (Derjaguin approximation) [15]. For instance when the AFM tip and the sample are modeled as a sphere with a radius R and a simple plane located at a distance d from the tip, respectively, EDL force F_EDL is expressed by

$$F_\mathrm{EDL} = \frac{2\pi R}{\varepsilon\kappa}\left[\left(\sigma_\mathrm{t}^2 + \sigma_\mathrm{s}^2\right)e^{-2\kappa d} + 2\sigma_\mathrm{t}\sigma_\mathrm{s}e^{-\kappa d}\right]\frac{1}{1-e^{-2\kappa d}}, \tag{19.10}$$

where σ_t and σ_s are the surface charge density of the tip and sample, respectively. EDL force was first intensively studied by Derjaguin, Landau, Verwey and Overbeek in connection with colloidal dispersions in electrolyte solutions. The addition of EDL force and van der Waals force (F_vdW) is called DLVO force, $F_\mathrm{DLVO}(= F_\mathrm{EDL} + F_\mathrm{vdW})$.

19.2 Quantitative Force/Dissipation Measurement Using FM-AFM in Liquids

19.2.1 Effect of Phase Shifting Elements in FM-AFM

Figure 19.2 shows a block diagram of FM-AFM instrument using an optical beam deflection sensor. In FM-AFM, a cantilever is oscillated by an excitation system, typically an acoustic excitation system using a piezoelectric actuator, driven by an excitation signal. The FM-AFM supplies the excitation signal such that the displacement signal reflecting the tip motion has a constant phase delay to the excitation

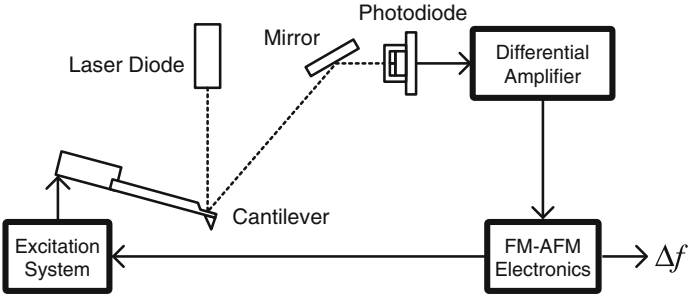

Fig. 19.2 Block diagram of FM-AFM using optical beam deflection sensor

signal. Thereby the frequency of the excitation signal matches the resonance frequency of the cantilever, and the resonance frequency of the cantilever is measured [1].

When the cantilever is excited indirectly by using a piezoelectric actuator in liquids, the actuator excites not only the base of the cantilever but causes unwanted vibration of surrounding components because the Q-factor of the cantilever is low. In such cases, the amplitude and phase transfer functions of the cantilever are distorted with spurious resonance peaks [16]. Moreover, other elements such as the displacement sensor or FM-AFM electronics may have frequency-dependent phase shift in the frequency range of the cantilever resonance frequency. Here we analyze the effect of these phase shifting elements (PSEs), which modify the phase versus frequency curve of the cantilever, on the signal and noise of the frequency shift in FM-AFM [11, 17].

The oscillation frequency of the cantilever is the frequency at which the phase criterion

$$\theta(f) + \theta_{\mathrm{E}}(f) = 2\mathrm{n}\pi \tag{19.11}$$

is met, where $\theta(f)$ is the phase transfer function of the cantilever and $\theta_{\mathrm{E}}(f)$ is the phase shift of the FM-AFM electronics. Since the phase shift of the cantilever at f_0, i.e. $\theta(f_0)$, is $-\pi/2$, $\theta_{\mathrm{E}}(f)$ is kept constant at $\pi/2 + 2\mathrm{n}\pi$ during experiments. However, due to the presence of the PSE, the phase criterion determining the oscillation frequency in actual FM-AFM instrument often becomes

$$\theta_{\mathrm{eff}}(f) + \theta_{\mathrm{E}}(f) = 2\mathrm{n}\pi, \tag{19.12}$$

where $\theta_{\mathrm{eff}}(f)$ is apparent phase transfer function with the presence of the PSE. Schematics of the phase transfer functions of the cantilever without any PSE ($\theta(f)$) and with the PSE ($\theta_{\mathrm{eff}}(f)$) are shown in Fig. 19.3a as thin and thick curves, respectively. Their slopes at f_0 are given by

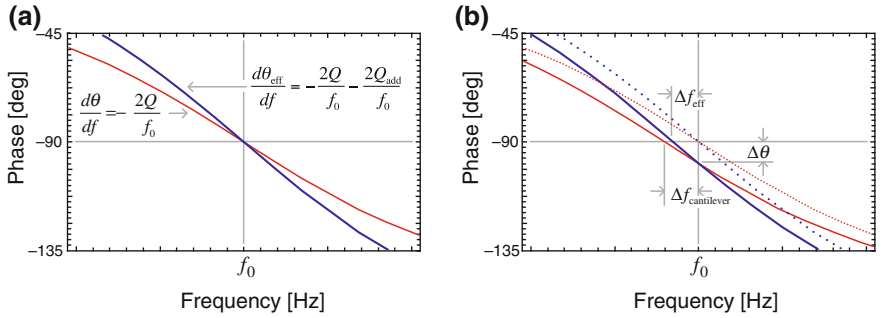

Fig. 19.3 **a** Schematic of apparent phase versus frequency curves of the cantilever without any PSE (*thin curve*) and with the PSE (*thick curve*). **b** Schematic illustration showing that the oscillation frequency deviates from the resonance frequency

$$\left.\frac{d\theta}{df}\right|_{f=f_0} = -\frac{2Q}{f_0} \tag{19.13}$$

and

$$\left.\frac{d\theta_{\rm eff}}{df}\right|_{f=f_0} = -\frac{2Q}{f_0} - \frac{2Q_{\rm add}}{f_0} = -\frac{2Q_{\rm eff}}{f_0}, \tag{19.14}$$

where Q and $Q_{\rm eff}$ are intrinsic and effective Q-factors, respectively. $Q_{\rm add}$ corresponds to the Q-factor of the PSE, which is defined by the slope of $\theta_{\rm add}$ at f_0. If we consider the situation where $\theta(f)$ is slightly shifted by $\Delta f_{\rm cantilever}$ due to the tip-sample interaction force, and the resonance frequency moves to $f_0 + \Delta f_{\rm cantilever}$, the phase response of the cantilever at f_0 shifts to $-\pi/2 + \Delta\theta$, where $\Delta\theta$ is given by

$$\Delta\theta = 2Q\frac{\Delta f_{\rm cantilever}}{f_0} \tag{19.15}$$

as shown in Fig. 19.3b. This phase shift is instantaneously nulled by the FM-AFM electronics, which adjust the oscillation frequency to $f_0 + \Delta f_{\rm cantilever}$. However, with the presence of the PSE, the phase shift $\Delta\theta$ is nulled by adjusting the oscillation frequency to $f_0 + \Delta f_{\rm eff}$, which is given by

$$\Delta f_{\rm eff} = \Delta\theta\left(\left|\frac{d\theta_{\rm eff}}{df}\right|_{f=f_0}\right)^{-1} = \frac{Q}{Q_{\rm eff}}\Delta f, \tag{19.16}$$

where $\Delta f_{\rm eff}$ represents the effective frequency shift tracked by the FM-AFM electronics with the presence of the PSE. This equation shows that the measured frequency shift is smaller than the actual frequency shift of the cantilever by a factor of $Q/Q_{\rm eff}$. Note that the signal to noise ratio of the FM-AFM is not affected by the PSE as the

equations for the frequency noises integrated over the measurement bandwidth with and without the PSE,

$$\delta f^{(\text{low-}Q)} = \frac{1}{A}\sqrt{\frac{f_0 k_\text{B} T B}{\pi k Q} + \frac{{f_0}^2 {N_\text{ds}}^2 B}{2Q^2}} \tag{19.17}$$

and

$$\delta f_\text{eff}^{(\text{low-}Q)} = \frac{1}{A}\sqrt{\frac{Q f_0 k_\text{B} T B}{\pi k Q_\text{eff}^2} + \frac{f_0^2 {N_\text{ds}}^2 B}{2{Q_\text{eff}}^2}} = \frac{Q}{Q_\text{eff}}\delta f^{(\text{low-}Q)}, \tag{19.18}$$

show that the frequency noise is also reduced by a factor of Q/Q_eff with the presence of the PSE.

19.2.2 Photothermal Excitation of Cantilevers in Liquids

Ideal amplitude and phase transfer functions of the cantilever are obtained by direct excitation methods such as magnetic [18] or photothermal excitation methods [19, 20]. While the former method requires attachment of magnetic particle or magnetic coating on the cantilever, the latter method can be readily applicable for any cantilevers without additional requirements.

Figure 19.4 shows a schematic diagram of the photothermal excitation system [17, 21]. We focused a blue-violet laser diode near the base of the cantilever, as shown in Fig. 19.4a. As the cantilever displacement is proportional to the incident laser power, the excitation signal is coupled to the laser drive current while the average drive current is regulated to keep the average incident power constant, as shown in Fig. 19.4b. Figure 19.4c shows the amplitude transfer functions of a Si cantilever (PPP-NCH) in water driven by acoustic excitation and photothermal excitation methods. While the transfer function obtained by the acoustic excitation method showed

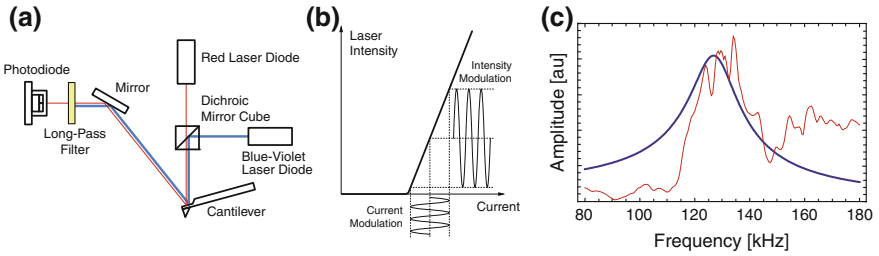

Fig. 19.4 **a** Schematic of photothermal excitation system. **b** Schematic of intensity versus laser current of laser diode for photothermal excitation. **c** Amplitude transfer functions of a cantilever in water by acoustic excitation and photothermal excitation

"forest of peaks" [16], that obtained by the photothermal excitation method showed the ideal damped harmonic oscillator response.

19.2.3 Optimum Oscillation Amplitude for FM-AFM in Liquids

The optimum oscillation amplitude of the cantilever for FM-AFM depends on the characteristic decay length of the interaction forces [22]. For nanometer-scale or atomic-scale topographic imaging in liquids, the characteristic decay length of the short-range repulsive force is on the order of a nanometer, and therefore the optimum oscillation amplitude is on the order of a nanometer. One can tune the oscillation amplitude to obtain the highest resolution images by using the procedures described below. On the other hand, the characteristic decay length of the hydration force is close to the size of the water molecules [2–4], and therefore the oscillation amplitude should be as small as the size of the water molecules or less, otherwise the oscillatory frequency shift as a function of the tip-sample distance is averaged out and not detectable.

Here we describe practical procedures to find the optimum oscillation amplitude for high-resolution topographic imaging by FM-AFM. First, the tip oscillated at a certain amplitude (a); e.g. 1 nm, is engaged to the sample surface in the constant frequency shift mode with a decent frequency setpoint. While acquiring some topographic images, the frequency setpoint is increased as high as possible ($\Delta f_{\max}$) before the cantilever oscillation becomes unstable. As the closest tip position during an oscillation cycle is now in a near-contact region, the tip position at which the frequency shift reaches $\Delta f_{\max}$ with a is defined as $z_{\min}$. Then we record the frequency shift versus distance curve from far above the surface to $z_{\min}$ under the same oscillation amplitude (a). The obtained frequency shift versus distance curve can be converted to the interaction force (F_{ts}) versus distance curve using the following equation [23],

$$F_{\mathrm{ts}}(z) = \frac{2k}{f_0}\int_z^{\infty}\left(\Delta f(\tau) + \frac{1}{8}\sqrt{\frac{a}{\pi(\tau - z)}}\Delta f(\tau) - \frac{a^{3/2}}{\sqrt{2(\tau - z)}}\frac{d\Delta f(\tau)}{d\tau}\right)d\tau. \tag{19.19}$$

The maximum interaction force in the curve corresponds to the interaction force exerted on the tip at $z_{\min}$ is defined as $F_{\max}$. From the force versus distance curve, the frequency shift versus distance curve for arbitrary oscillation amplitudes (A) can be simulated using the following equation [23, 24],

$$\Delta f(A, z) = -\frac{f_0}{\pi A k_z}\int_{-1}^{1} F(z + A(1 + u))\frac{u}{\sqrt{1 - u^2}}du. \tag{19.20}$$

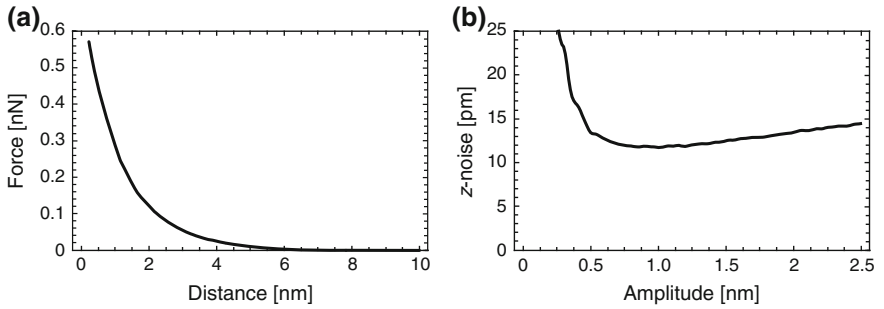

Fig. 19.5 **a** Force versus distance curve measured on bacteriorhodopsin protein molecules. **b** z-noise during high-resolution imaging of bacteriorhodopsin protein molecules calculated using the experimental parameters and force versus distance curve

Then the frequency shift at the closest tip distance ($z_{\min}$) is calculated as the maximum frequency shift in the simulated curve for arbitrary oscillation amplitudes as $\Delta f_{\max}(A)$. As the frequency noise is inversely proportional to the oscillation amplitude (A), as shown in (19.17), one can calculate z-noise at $z_{\min}$, defined as $\delta z = \delta f/(\partial \Delta f_{\max}(A)/\partial z)$ [22].

Figure 19.5a is a force versus distance curve measured on bacteriorhodopsin protein molecules in a purple membrane using a Si cantilever (PPP-NCH) [25]. z-noise was calculated as a function of the oscillation amplitude and plotted in Fig. 19.5b, showing the optimum oscillation amplitude is about 1 nm.

19.2.4 2D and 3D Force Mapping Techniques

The 2D/3D force mapping techniques are similar to those called force curve imaging spectroscopy [26] or force mapping [27]. The 3D mapping of the cantilever frequency shift by FM-AFM has been demonstrated in vacuum at low temperatures, by measuring a frequency shift versus tip-sample distance curve at individual pixels on the sample surface [28], and by obtaining a 2D frequency shift image at various tip-sample distances [29]. On the other hand, since the tip-sample distance feedback control should be disabled in both methods, it has been difficult to perform 3D frequency shift mapping by FM-AFM working in liquids without affected by the thermal drift. To overcome this problem, we implemented drift correction and tip retraction functions in the control software.

Procedures of 3D frequency shift mapping in our AFM system are schematically shown in Fig. 19.6. The tip was engaged to the sample surface, and the tip-sample distance was controlled by keeping the frequency shift constant. A slow ramp signal was added to the scan signals of the sample scanner for linear drift correction throughout the measurements [30]. After the tip-sample distance feedback control was disabled, and 2D frequency shift maps in z–x planes which are slightly separated in y direction

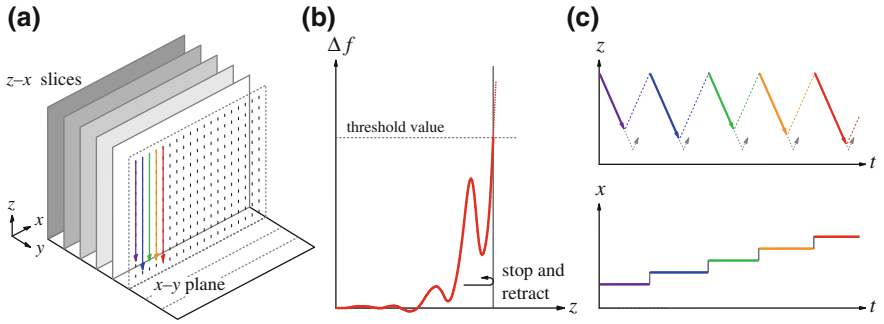

Fig. 19.6 **a** 3D frequency shift data was collected by performing 2D frequency shift mapping in z–x planes which are slightly separated in y direction. **b** In each frequency shift curve measurement, the tip was retracted immediately if the frequency shift reached the threshold value. **c** Timing charts during 2D frequency shift mapping

were collected as shown in Fig. 19.6(a). At each x position, the frequency shift versus distance curve was recorded while the tip was approached to the sample surface by applying a ramp signal to z piezo. The ramp signal was immediately stopped when the frequency shift signal reached a predetermined threshold value, and the tip was retracted to the original position as shown in Fig. 19.6b, c. This threshold frequency shift was determined at the maximum in the range where the frequency shift curves could be reproducibly collected; if the threshold frequency shift was set at a larger value than this, the measurements were not reliable because of unstable cantilever oscillation or tip change.

19.3 Application of FM-AFM 1: 2D/3D Force Mapping

19.3.1 3D Hydration Force Mapping on Muscovite Mica

We first demonstrated visualization of structured water layers by performing 2D frequency shift mapping by FM-AFM on a mica surface and a graphite surface, and on bacteriorhodopsin proteins in a purple membrane [4, 31]. However, precise comparison of the experimental data with theoretically calculated hydration structures or hydration forces [32, 33] requires 3D data, which allows us to identify the relationship between the atomic and molecular species on the surfaces and their specific hydration structures.

We performed 3D frequency shift mapping on a cleaved muscovite mica in 1 mol/l KCl solution. A Si cantilever (PPP-NCHAuD) was used with a constant oscillation amplitude of 0.24 nm peak-to-peak. We collected 67 slices of 2D frequency map (z–x slice). The threshold frequency shift (see Sect. 19.2.4) was set to 2250 Hz, which corresponded to the interaction force of about 0.4 nN. The 3D data set with dimensions of 3 nm (x) × 2.3 nm (y) × 1.6 nm (z) was obtained in 168 s [3].

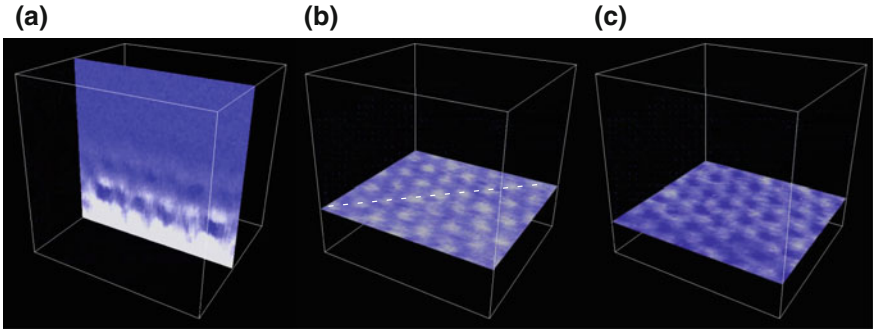

Fig. 19.7 Snapshots from movie files of 3D frequency shift map obtained on muscovite mica in aqueous solution

Figure 19.7 shows snapshots from movie files of the 3D frequency shift map. Figure 19.7a is a z–x slice, as originally obtained in the experiments. The z–x slice shows complicated contrasts reflecting 2D hydration structures. Figure 19.7b, c are x–y slices, reconstructed from the 3D frequency shift data, show variations of the frequency shift in x–y planes, namely a dot-like pattern and a honeycomb-like pattern, respectively. The separation of the two x–y slices in z direction was 0.2 nm.

Figure 19.8a shows a 2D frequency shift map in the z–x plane including the dotted line in Fig. 19.7b, which crosses the bright dots of the dot-like pattern. The locations of the two x–y slices in Fig. 19.7b, c are indicated by the triangles. In this figure, it becomes clear that the dark contrasts are beneath the bright dots, namely the inversion of the contrast.

We compared the 3D frequency shift data and force data to theoretical 3D data of atomic distribution of water molecules by a statistical-mechanical theory of solvation, known as 3D-RISM theory [4, 15]. The surface of the mica model used in the 3D-RISM calculation is shown in Fig. 19.8b. We found the oxygen density also shows similar dot-like and honeycomb-like patterns with a separation of about 0.2 nm with each other. Two x–y slices reconstructed from the 3D oxygen density data are shown in Fig. 19.8c, d. These x–y slices show variation of the oxygen density which is equivalent to the water molecule density. The honeycomb-like pattern follows locations of the surface atoms while the dots in the dot-like pattern are on the hollow sites. Figure 19.8e shows a 2D oxygen density map in the z–x plane including the dotted line in Fig. 19.8c, which crosses the bright dots of the dot-like pattern. The locations of the two x–y slices in Fig. 19.8c, d are indicated by the triangles in the same way as the experimental result. Here the inversion of the contrast between Fig. 19.8c, d were represented, which showed a good agreement with the experimental result.

Figure 19.9a shows an averaged frequency shift versus distance curve in for all pixels in x–y plane. There are three distinct maxima in the averaged frequency shift curve, at $z = 0.5$–0.6 nm, $z = 0.9$–1.0 nm, and $z = 1.4$ nm. An averaged force versus distance curve was also plotted in the figure. The triangles in the plot indicate the locations at which the dot-like and honeycomb-like patterns were obtained.

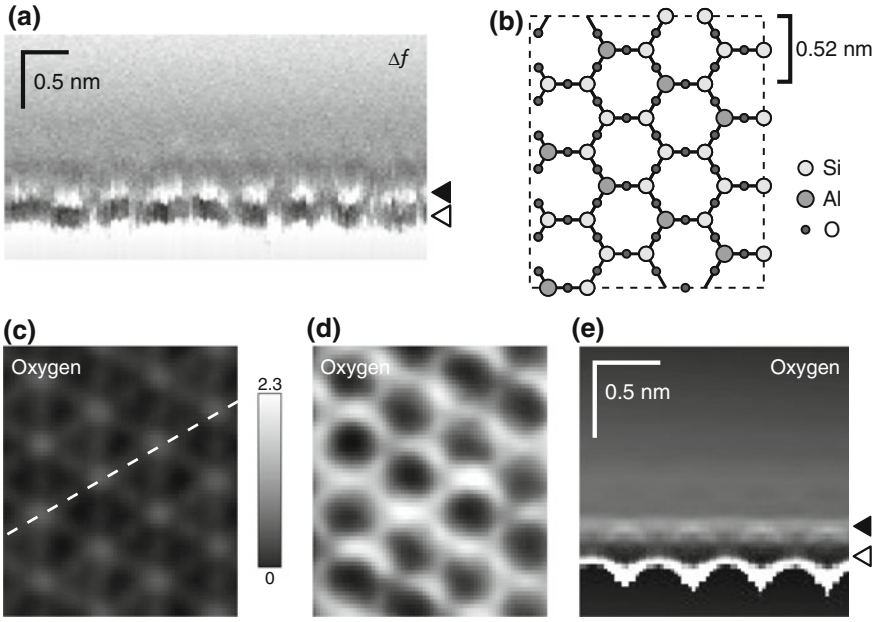

Fig. 19.8 **a** 2D frequency shift map in the *z*–*x* plane including the *dotted line* in Fig. 19.7b. **b** Schematic of surface atoms of the muscovite mica model. **c**, **d** are calculated 2D oxygen density maps showing *dot-like* and *honeycomb-like* features. **e** Calculated 2D oxygen density map in the *z*–*x* plane including the *dotted line* in (**c**)

Figure 19.9b is an averaged normalized oxygen density profile as a function of the distance from the surface atoms obtained by the 3D-RISM calculation. The locations of the maxima and minima in Fig. 19.9b well correspond to those in Fig. 19.9a, namely the maxima in the frequency shift or force correspond to the hydration layers, in which the water densities are greater than the bulk density.

The frequency shift maximum in the averaged frequency shift curve at $z = 0.5$–0.6 nm corresponds to the hydration layer in the 3D-RISM data, which was also reported by the X-ray crystal truncated rod measurement and referred to as the second hydration layer [34]. The dot-like pattern reflects the lateral structures of the second hydration layer, while the honeycomb-like pattern reflects the lateral structures of the first layer. We consider that it would be difficult to visualize the adsorbate layer by FM-AFM because the tip should pick the ditrigonal cavity and displace the water molecule inside, which is not probable with a tip of a radius on the order of nanometers, as simulated by the MD calculation [32].

Figure 19.10a is the *x*–*y* slice reconstructed from the 3D force data, at the tip-sample separation same as that in Fig. 19.7b. The interaction force versus distance curve on the site 1 corresponding to the honeycomb core of the mica surface, that on the site 2 corresponding to the bridge site, and that on the site 3 corresponding to Si or Al site were plotted in Fig. 19.10b. We found all these curves are qualitatively similar to those by the MD simulation.

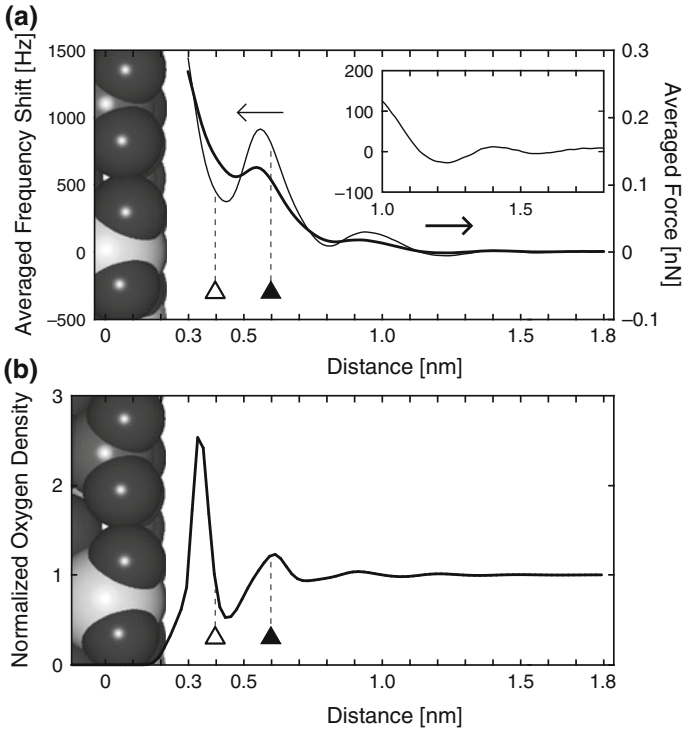

Fig. 19.9 **a** Averaged frequency shift versus distance curve and averaged force versus distance curve on mica surface. *Inset* shows a magnified frequency shift curve to clearly show the oscillatory features. **b** Normalized oxygen density profile derived by averaging 3D oxygen density map obtained by the 3D-RISM calculation

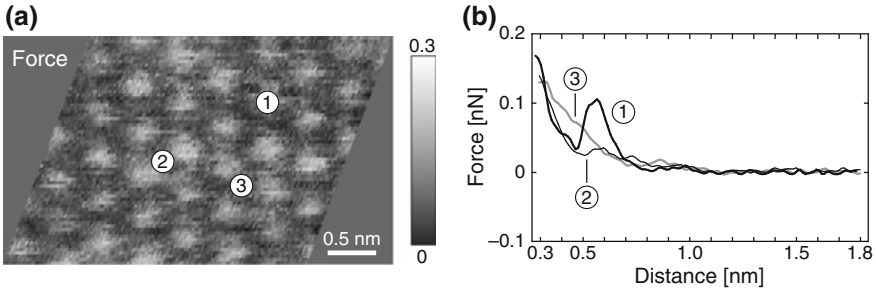

Fig. 19.10 **a** 2D force map (*x*–*y* slice) at the same tip-sample separation of Fig. 19.7b, reconstructed from the 3D force data. **b** Site-specific interaction force versus distance curves on the locations indicated in (**a**)

19.3.2 3D Electrostatic Force Mapping on Surfactant Aggregates

We applied the 3D force mapping method using FM-AFM to the investigation of the surface charge distribution and the structures of self-assembled surfactant aggregates at graphite aqueous solution interfaces [5]. We successfully visualized the 3D EDL force on the surface aggregates with molecular-scale resolution and obtained the local variation in the surface charge density on the aggregate by fitting the experimental 2D force map to the theoretical 2D EDL force map.

We deposited an aqueous solution of sodium dodecyl sulfate (SDS), $CH_3(CH_2)_{11}OSO_3^-Na^+$, on a cleaved graphite surface. A Si cantilever (PPP-NCH) was oscillated with the photothermal excitation method (see Sect. 19.2).

Figure 19.11a, b show FM-AFM images of a graphite substrate covered with SDS self-assemblies. The stripe structures having a spacing of about 4.8 nm were imaged with a domain boundary. According to the previous studies [35, 36], the SDS molecules are expected to form hemicylindrical surface micelles on the graphite surface with their hydrophilic head groups protruding outward and their sodium cations partially dissociated, as shown in Fig. 19.11b.

Figure 19.12 shows a 3D frequency shift map obtained at the interface between a graphite surface and an SDS aqueous solution (34 mM). The bright contrast of the image corresponds to the magnitude of the positive frequency shift. When the tip was brought closer to the micelle surface from a position located far from the surface, the repulsive force exponentially increased with the distance, which is a characteristic of the EDL force, until the tip penetrated the micelle surface. Although the tip penetrated the micelle surface at each frequency shift curve measurement, the obtained curves were highly reproducible, which means that the micelle structure was immediately recovered after each tip retraction. In fact each retract frequency shift curve was almost completely overlapped with the corresponding approach curve. In the 3D map, the hemicylindrical structure of the SDS aggregates was clearly visualized as a boundary between the bright and dark regions. In the reconstructed x–y slice at the distance closer to the graphite surface after the tip penetration, the parallel stripe

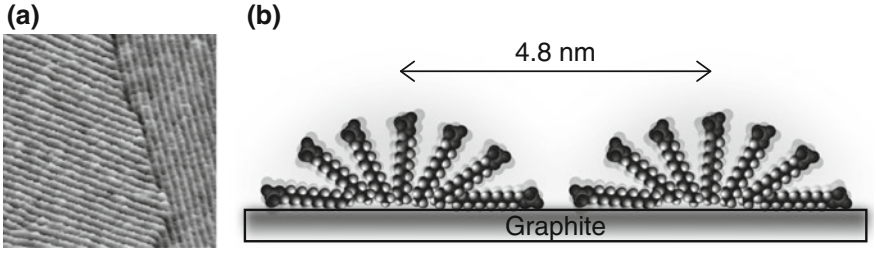

Fig. 19.11 **a** Topographic FM-AFM image of SDS self-assembled aggregates on graphite (Scan range: 133 nm × 133 nm). **b** Schematic of hemicylindrical SDS aggregates formed on graphite surface

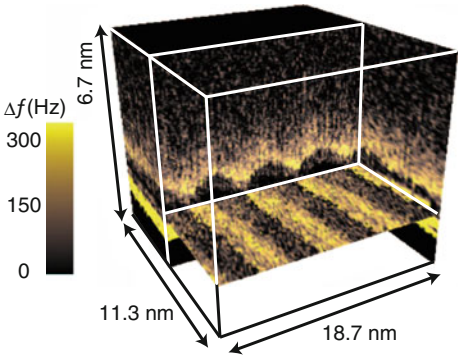

Fig. 19.12 Snapshot from a movie of 3D frequency shift map obtained at the interface between a graphite surface and an SDS aqueous solution

features were observed, suggesting that the SDS molecules were rearranged by the tip to form molecular layers parallel to the graphite surface.

We modeled the tip and the SDS aggregates, and then the EDL force between a spherical tip and an arbitrary shape is calculated at each tip location based on the single-layer potential method for the linearized Poisson-Boltzmann equation, which allows us to obtain a theoretical 3D EDL force map. Finally, the theoretical force map is fitted to the experimental data to find the surface charge density distribution function on the SDS aggregates. As the structure is uniform in the longitudinal axis of the hemicylinder and the charge density distribution was obviously periodic, the single layer potential function can be expanded as a Fourier series. The 2D EDL force map extracted from the theoretical 3D EDL force map was fitted to the experimentally obtained 2D force map. Figure 19.13 shows a surface charge density distribution on the SDS aggregate calculated from the fitting parameters that gave the

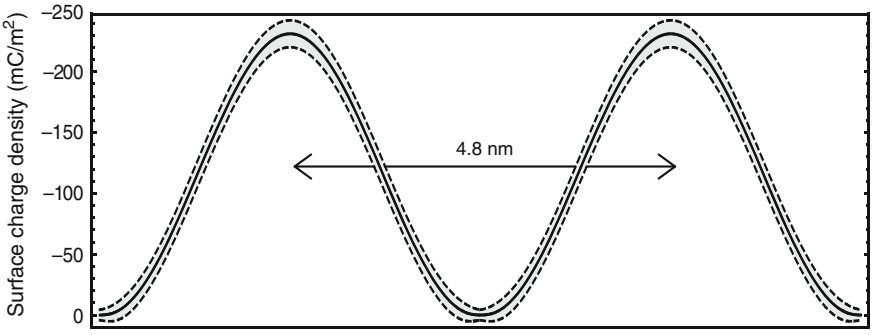

Fig. 19.13 Surface charge density distribution on SDS aggregates obtained from the force curves fitted to the experimental data. *Shaded area* represents the error in the charge density distribution estimated by taking the measurement noise in the force data into account

best fit. The variation in the charge density distribution is (grey region) also shown. This figure shows that the surface charge density on the SDS aggregate varies from 0 to $-250\mathrm{mC/m^2}$ depending on the position on a molecular scale.

19.4 Application of FM-AFM 2: High-Resolution Imaging of Biomolecules

19.4.1 DNA

It has been well known that most double-stranded DNA (dsDNA) molecules adopt the B-form conformation under physiological conditions. B-form DNA (B-DNA) molecules have right-handed helical structures and distinctive major and minor grooves, which are ideally described by the Watson-Crick model of DNA [37].

Bacterial plasmid pUC18 (2686 base pairs), which is a closed circular DNA, was immobilized onto a freshly cleaved muscovite mica substrate and FM-AFM imaging was performed in 50 mM $NiCl_2$ solution. Because both the cleaved surface of muscovite mica and the sugar-phosphate backbone are negatively charged, nickel ions weakly bind DNA onto the mica substrate by electrostatic interactions [38]. The tip-sample distance was regulated by keeping the frequency shift constant at about +80 Hz, which corresponds to the tip-sample interaction force of about +40 pN.

A typical FM-AFM topographic image of the plasmid DNA in 50 mM $NiCl_2$ solution is shown in Fig. 19.14. The plasmid DNA molecules are interwound, as previously reported [39]. Figure 19.15 is a high-resolution FM-AFM image of the plasmid DNA, which was obtained in the area indicated by the rectangle in Fig. 19.14. The measured height of the DNA backbones from the substrate was about 2 nm,

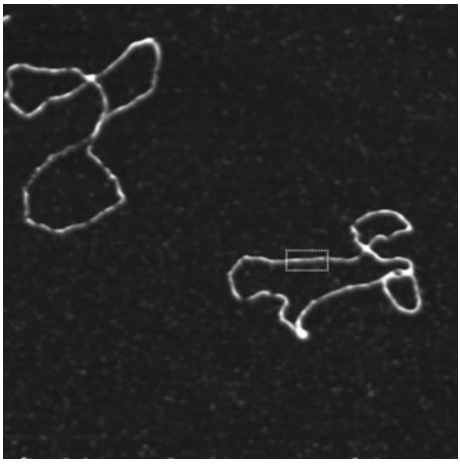

Fig. 19.14 FM-AFM image of plasmid DNA in aqueous solution (50 mM $NiCl_2$) (Scan range: 540 nm × 540 nm)

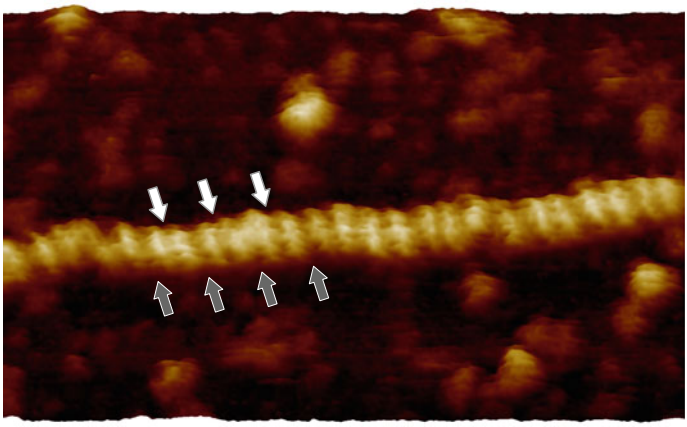

Fig. 19.15 FM-AFM image of plasmid DNA in aqueous solution (50 mM $NiCl_2$) (Scan range: 48 nm × 20 nm)

which agrees well with the diameter of B-DNA (2.0 nm). There are a lot of globular features around the plasmid DNA which are assumed to be the adsorbates, as the mica surface was often partially covered with adsorbates from the $NiCl_2$ solution, such as nickel hydroxides, $Ni(OH)_2$. In this figure, deep grooves between the sugar-phosphate backbones of DNA are clearly resolved. We found that two distinct types of grooves with different widths appeared alternately, as partly indicated by white and grey arrows in Fig. 19.15, respectively. By carefully measuring the groove widths (distances between the adjacent DNA backbones) along the local helix axis of the DNA, two groove widths were quantitatively differentiated. These grooves are attributed to the major and minor grooves of B-DNA. The sum of the major and minor groove widths, which correspond to the B-DNA helix pitch, was 3.7 nm with a standard deviation of 0.15 nm. The helix pitch of B-DNA in water has been reported to be 3.6 nm (axial rise: 10.5 bp/turn on average [40]), and this value was determined to be slightly larger than that of the classic Watson-Crick model (3.4 nm) on the basis of an X-ray fiber diffraction study [37]. In addition, plasmid DNA isolated from cells is regularly underwound (negatively supercoiled) [41]. Therefore, we conclude that the helix pitch of 3.7 nm observed in our study reflects the nature of real plasmid DNA under physiological conditions.

We also performed the 2D frequency shift mapping on the plasmid DNA. Figure 19.16 is an FM-AFM topographic image of the plasmid DNA in 50 mM $NiCl_2$ solution. Along the A-B line indicated in the figure, we obtained a 2D frequency shift map shown in Fig. 19.16b. On the plasmid DNA, a very complicated pattern was observed, which reflects the complex distribution of the water molecules around the DNA. On the other hand, stripe patterns parallel to the surface contour were observed on the surrounding adsorbates, which are presumably from nickel chloride solution.

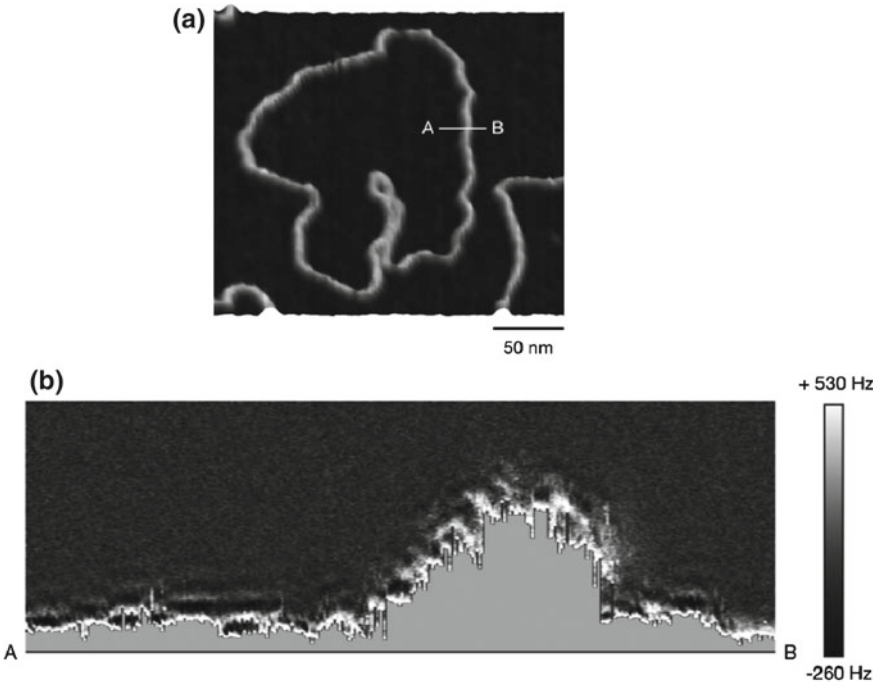

Fig. 19.16 2D frequency shift mapping of plasmid DNA in aqueous solution (50 mM $NiCl_2$). **a** FM-AFM image of plasmid DNA (Scan range: 100 nm × 82 nm). **b** 2D frequency shift map obtained along the *A-B line* in (**a**)

19.4.2 Self-assembled Monoclonal Antibodies

Antibodies are protein molecules that play a critical role in humoral immunity. Immunoglobulin G (IgG, 150 kDa) is one of the five isotypes of antibodies (IgA, IgD, IgE, IgG and IgM) and is most abundant in the serum. IgG molecules have Y-shaped structures with three arms, including two antigen-binding fragments (Fab regions) and one crystallizable fragment (Fc region). The Fab and Fc regions are connected via hinge regions, which contain conformationally flexible polypeptide chains, as shown in Fig. 19.17.

Anti-human serum albumin (HSA) mouse monoclonal antibodies (IgG1 isotype) were immobilized onto a freshly cleaved muscovite mica substrate, and FM-AFM imaging was performed in an electrolyte solution. Because both the cleaved surface of mica and IgG molecules are negatively charged at a neutral pH, cations weakly bind IgG molecules on the mica substrate via electrostatic interactions [38]. Figure 19.17b shows an FM-AFM image of an IgG molecule in 50 mM $ZnCl_2$. In this solution, IgG molecules with various conformations were individually adsorbed onto the mica substrate. Because isolated molecules have conformational flexibilities, they can

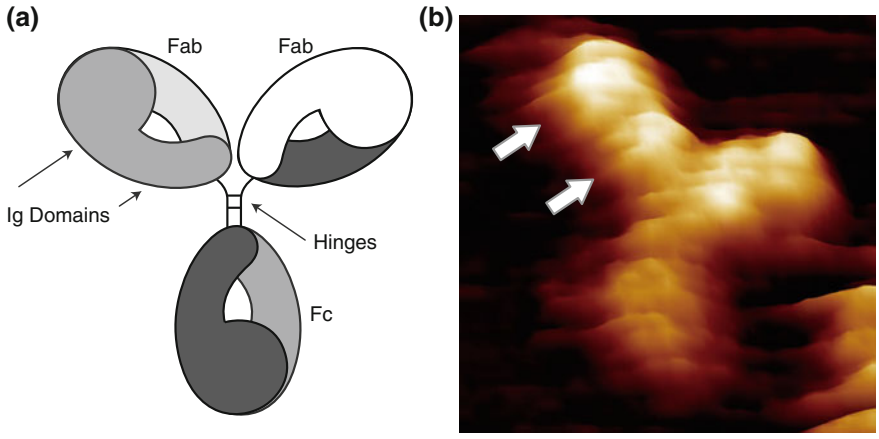

Fig. 19.17 **a** Ideal structural model of IgG molecule. **b** FM-AFM image of mouse monoclonal antibody (IgG1) in aqueous solution (50 mM $ZnCl_2$) (Scan range: 23 nm × 23 nm)

exhibit various binding structures when they are adsorbed on a substrate. The figure shows the three arms of IgG, reflecting its Y-shaped structure. We found that the heights of the two upper arms in Fig. 19.17b measured from the substrate were slightly higher than that of the remaining arm, based on which we assigned these two arms as Fab regions. We also identified two globular structures within each Fab region, as indicated by the arrows in Fig. 19.17b. These structures were assigned as immunoglobulin (Ig) domains, which are protein domain structures, and were composed of beta-sheet secondary structures (β-barrels).

We found that monoclonal IgG molecules self-assembled into well-ordered oligomers in aqueous solution. Figure 19.18a shows an FM-AFM image of IgG molecules in 50 mM $MgCl_2$. Under these conditions, we routinely observed flower-like structures with a diameter of approximately 30 nm. The hexamer formed by the self-association of six Fc regions via lateral Fc–Fc interactions [42, 43]. The Fc regions formed a donut-like inner assembly area at the center of the hexamer, and the outer petal-like structures were composed of six pairs of Fab regions. The two Fab regions in each petal belonged to different IgG molecules, as discussed below (see Fig. 19.19). Interestingly, the self-assembled IgG hexamer resembled IgM antibodies, which form donut-like pentamers, in which Fc regions are located at the centre of the oligomer and Fab regions stretched outward.

We also discovered that IgG hexamers self-assembled into ordered 2D crystals in aqueous solution, as shown in Fig. 19.18b. The mica substrate was fully covered with hexagonally arranged IgG hexamers with a lattice constant of 28 nm. We presumed that the 2D crystallization of IgG hexamers was induced by lateral Fab–Fab interactions among four Fab regions [44, 45]. Based on the height of the hexamers from the substrate, we concluded that only a monolayer (2D) crystal is formed and multi-layer (3D) crystallization does not occur on the mica substrate.

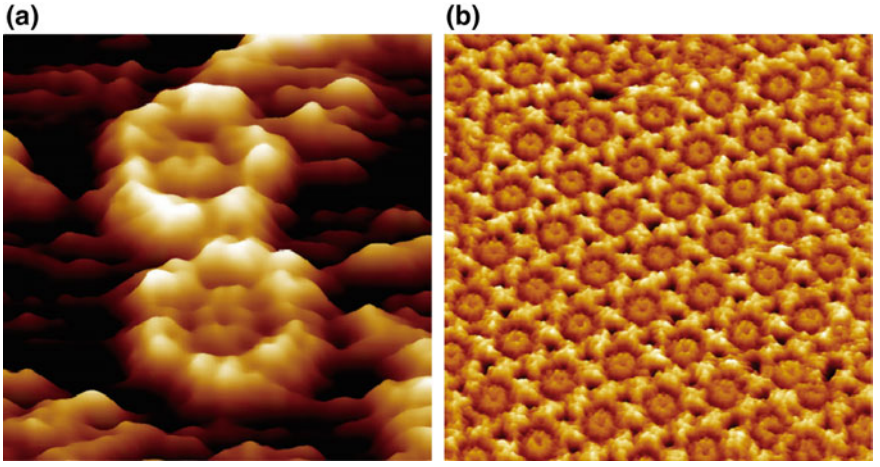

Fig. 19.18 **a** FM-AFM image of hexamers of mouse monoclonal antibody (IgG1) in aqueous solution (50 mM $MgCl_2$) (Scan range: 80 nm × 80 nm). **b** FM-AFM image of hexamers of mouse monoclonal antibody (IgG1) in aqueous solution (50 mM $MgCl_2$) (Scan range: 200 nm × 200 nm)

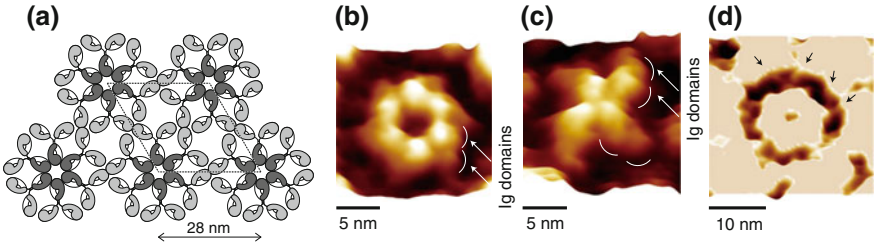

Fig. 19.19 **a** Structural model of self-assembled 2D IgG crystals determined by FM-AFM observation. **b–d** are FM-AFM images of self-assembly of six Fc regions in a 2D IgG crystal in aqueous solution (50 mM $MgCl_2$)

Figure 19.19a is a schematic of a structural model of the self-assembled 2D IgG crystals determined by FM-AFM observation. In this schematic, Fc and Fab regions are depicted as a comma-shaped model and a mirrored-comma shape, respectively, reflecting the different shapes of the regions. Using these models, the six-Fc assembly in the center of the hexamer, shown in Fig. 19.19b, can be represented as six comma shapes. In contrast, the four-Fab regions, shown in Fig. 19.19c, can be depicted as four mirrored-comma shapes. In Fig. 19.19b, c, pairs of globular structures corresponding to Ig domains within the Fc and Fab regions were also resolved, as indicated by the white arrows. In the deep circular groove surrounding the six-Fc assembly, several pairs of single polypeptide chains in the hinge regions were also resolved in the contrast-enhanced FM-AFM image shown in Fig. 19.19d, as indicated by the black arrows.

19.5 Summary and Outlook

This chapter has focused mainly on recent, rapid progress in FM-AFM in liquids. The 2D/3D force mapping based on the quantitative force curve measurement is a powerful, promising technique having a wide variety of applications to molecular-scale solid-liquid interface studies. The required conditions for the quantitative force measurement in liquids were specifically explained. The photothermal excitation of the cantilever oscillation is extremely suitable for obtaining the ideal amplitude and phase transfer functions, satisfying these conditions. In addition we showed the applications of 2D/3D force mapping to the molecular-scale visualization of hydration structures on muscovite mica. The results indicated that the water molecule density over the mica surface is modulated, directly reflecting the surface crystal site. The electric double layer force on surfactant aggregates was also three-dimensionally visualized, which allowed us to obtain nanometer-scale surface charge distribution on the aggregates. Furthermore, high-resolution FM-AFM images of biological molecules such as double-helix structure of DNA and hexamers of IgG antibody molecules obtained in quasi-physiological environments were presented.

Although the force versus distance curve measurement with the aid of the DLVO theory enables us to precisely study local EDL force analysis, which can basically give us the surface charge information, the method is not necessarily applied to general surface charge/potential studies. This is because charging processes at solid-liquid interfaces are quite complicated, including protonation/deprotonation phenomena and cation adsorption/desorption. In addition, the electrical state on the tip surface can significantly affect the surface charge of the sample. Chemical and/or electrochemical control of the tip surface might be necessary for further studies.

Recent, amazing progress in super high-resolution FM-AFM imaging of molecules using a molecule (CO) tip in ultrahigh-vacuum conditions at a low temperature has brought a novel insight into single-molecule science [46, 47]. Although its experimental environment is completely different from the liquid FM-AFM measurement, it must be a good opportunity for us to reconsider the possibility of breaking through the present imaging resolution in liquids.

References

1. T.R. Albrecht, P. Gruütter, P. Horne, D. Rugar, J. Appl. Phys. **69**, 668 (1991)
2. A. Labuda, K. Kobayashi, D. Kiracofe, K. Suzuki, P.H. Grütter, H. Yamada, AIP Adv. **1**, 022136 (2011)
3. K. Kobayashi, N. Oyabu, K. Kimura, S. Ido, K. Suzuki, T. Imai, K. Tagami, M. Tsukada, H. Yamada, J. Chem. Phys. **138**, 184704 (2013)
4. K. Kimura, S. Ido, N. Oyabu, K. Kobayashi, Y. Hirata, T. Imai, H. Yamada, J. Chem. Phys. **132**, 194705 (2010)
5. K. Suzuki, K. Kobayashi, N. Oyabu, K. Matsushige, H. Yamada, J. Chem. Phys. **140**, 054704 (2014)

6. S. Ido, K. Kimura, N. Oyabu, K. Kobayashi, M. Tsukada, K. Matsushige, H. Yamada, ACS Nano **7**, 1817 (2013)
7. S. Ido, H. Kimiya, K. Kobayashi, H. Kominami, K. Matsushige, H. Yamada, Nat. Mater. **13**, 264 (2014)
8. J.E. Sader, J. Appl. Phys. **84**, 64 (1998)
9. C.P. Green, J.E. Sader, J. Appl. Phys. **98**, 114913 (2005)
10. A. Maali, C. Hurth, R. Boisgard, C. Jai, T. Cohen-Bouhacina, J.P. Aime, J. Appl. Phys. **97**, 074907 (2005)
11. K. Kobayashi, H. Yamada, K. Matsushige, Rev. Sci. Instrum. **80**, 043708 (2009)
12. T. Fukuma, M. Kimura, K. Kobayashi, K. Matsushige, H. Yamada, Rev. Sci. Instrum. **76**, 053704 (2005)
13. M. Watkins, B. Reischl, J. Chem. Phys. **138**, 154703 (2013)
14. A. Kovalenko, F. Hirata, J. Chem. Phys. **110**, 10095 (1999)
15. J.N. Israelachivili, *Intermolecular and Surface Forces*, 3rd edn. (Academic Press, London, 2011)
16. T. Schäffer, J.P. Cleveland, F. Ohnesorge, D.A. Walters, P.K. Hansma, J. Appl. Phys. **80**, 3622 (1996)
17. K. Kobayashi, H. Yamada, K. Matsushige, Rev. Sci. Instrum. **82**, 033708 (2011)
18. S.P. Jarvis, A. Oral, T.P. Weihs, J.B. Pethica, Rev. Sci. Instrum. **64**, 3515 (1993)
19. N. Umeda, S. Ishizaki, H. Uwai, J. Vac. Sci. Technol. B **9**, 1318 (1990)
20. G.C. Ratcliff, D.A. Erie, R. Superfine, Appl. Phys. Lett. **72**, 1911 (1998)
21. D. Kiracofe, K. Kobayashi, A. Labuda, A. Raman, H. Yamada, Rev. Sci. Instrum. **82**, 013702 (2011)
22. F. Giessibl, H. Bielefeldt, S. Hembacher, J. Mannhart, Appl. Surf. Sci. **140**, 352 (1999)
23. J.E. Sader, S.P. Jarvis, Appl. Phys. Lett. **84**, 1801 (2004)
24. F. Giessibl, Phys. Rev. B **56**, 16010 (1997)
25. H. Yamada, K. Kobayashi, T. Fukuma, Y. Hirata, T. Kajita, K. Matsushige, Appl. Phys. Express **2**, 095007 (2009)
26. D.R. Baselt, J.D. Baldeschwieler, J. Appl. Phys. **76**, 33 (1994)
27. D.E. Laney, R.A. Garcia, S.M. Parsons, H.G. Hansma, Biophys. J. **72**, 806 (1997)
28. A. Schwarz, H. Hölscher, S.M. Langkat, R. Wiesendanger, AIP Conf. Proc. **696**, 68 (2003)
29. B.J. Albers, T.C. Schwendemann, M.Z. Baykara, N. Pilet, M. Liebmann, E.I. Altman, U.D. Schwarz, Nat. Nanotechnol. **4**, 307 (2009)
30. D. Sawada, Y. Sugimoto, K. Morita, M. Abe, S. Morita, Appl. Phys. Lett. **94**, 173117 (2009)
31. K. Suzuki, N. Oyabu, K. Kobayashi, K. Matsushige, H. Yamada, Appl. Phys. Express **4**, 125102 (2012)
32. M. Tsukada, N. Watanabe, M. Harada, K. Tagami, J. Vac. Sci. Technol. B **28**, C4C1 (2010)
33. M. Watkins, A.L. Shluger, Phys. Rev. Lett. **105**, 196101 (2010)
34. L. Cheng, P. Fenter, K.L. Nagy, M.L. Schlegel, N.C. Sturchio, Phys. Rev. Lett. **87**, 156103 (2001)
35. E.J. Wanless, W.A. Ducker, J. Phys. Chem. **100**, 3207 (1996)
36. V.K. Paruchuri, J. Nalaskowski, D.O. Shah, J.D. Miller, Colloids Surf. A **272**, 157 (2006)
37. J.D. Watson, F.H.C. Crick, Nature **171**, 737 (1953)
38. H.G. Hansma, D.E. Laney, Biophys. J. **70**, 1933 (1996)
39. H.G. Hansma, Science **256**, 1180 (1992)
40. D. Rhodes, A. Klug, Nature **286**, 573 (1980)
41. T.C. Boles, J.H. White, N.R. Cozzarelli, J. Mol. Biol. **213**, 931 (1990)
42. L. Pinteric, R.H. Painter, G.E. Connell, Immunochemistry **8**, 1041 (1971)
43. D.R. Burton, Mol. Immunol. **22**, 161 (1985)
44. H. Yagi, N. Takahashi, Y. Yamaguchi, K. Kato, Mol. Immunol. **41**, 1211 (2004)
45. S. Kanai, J. Liu, T.W. Patapoff, S.J. Shire, J. Pharm. Sci. **97**, 4219 (2008)
46. L. Gross, F. Mohn, N. Moll, P. Liljeroth, G. Meyer, Science **325**, 1110 (2009)
47. L. Gross, F. Mohn, N. Moll, G. Meyer, R. Ebel, W.M. Abdel-Mageed, M. Jaspars, Nat. Chem. **2**, 821 (2010)